Retrieval of Mars surface physical properties from OMEGA hyperspectral images using Regularized Sliced Inverse Regression

Caroline Bernard-Michel, Sylvain Douté, Mathieu Fauvel, Laurent Gardes, Stéphane Girard

Retrieval of Mars surface physical properties from OMEGA hyperspectral images using regularized sliced inverse regression

C. Bernard-Michel,[1] S. Douté,[2] M. Fauvel,[1] L. Gardes,[1] and S. Girard[1]

Received 21 April 2008; revised 12 February 2009; accepted 20 March 2009; published 19 June 2009.

[1] In this paper, a method based on modeling and statistics is proposed to evaluate the physical properties of surface icy materials on Mars from hyperspectral images collected by the OMEGA instrument aboard the Mars Express spacecraft. The approach is based on the estimation of the functional relationship F between observed spectra and relevant physical parameters such as compound abundances and granularity. To this end, a database of synthetic spectra is generated by a radiative transfer model simulating the reflection of solar light by a granular mixture of H_2O ice, CO_2 ice, and dust. The database constitutes a training set used to estimate F. The high dimension of spectra is reduced by Gaussian regularized sliced inverse regression (GRSIR) to overcome the ''curse of dimensionality'' and, consequently, the sensitivity of the inversion to noise (ill-conditioned problems). Compared with other approaches, such as the k-NN, the partial least squares, and the support vector machines (SVM), GRSIR has the advantage of being very fast, interpretable, and accurate. For instance, on simulated test data, the same level of accuracy is obtained by GRSIR and SVM for the estimation of the proportion of dust with a normalized root-mean-square error of 13%, but GRSIR performs 100 times faster. On real data, parameter maps generated by GRSIR from a sequence of three OMEGA observations of the bright permanent polar cap (BPPC) are much smoother, detailed, and coherent than with other competing methods. They indicate that coarse-grained dry ice completely dominates (≈99.55–99.95 wt%) the material forming the top few centimeters of the BPPC with dust and water only present as traces (from 300 to 1000 ppm). The maps show clear regional variations of water and dust contamination as well as CO_2 ice state of densification (mean free path around 5 cm on the average, with variations of ±50%) that must be related to meteorological and microphysical phenomena.

Citation: Bernard-Michel, C., S. Douté, M. Fauvel, L. Gardes, and S. Girard (2009), Retrieval of Mars surface physical properties from OMEGA hyperspectral images using regularized sliced inverse regression, *J. Geophys. Res.*, *114*, E06005, doi:10.1029/2008JE003171.

1. Introduction

[2] Visible and infrared imaging spectroscopy is a key remote sensing technique used to study and monitor planets. It allows the detection, mapping and characterization of minerals, as well as volatile species, whose presence often provide clues for the resolution of key climatic and geological issues [*Murchie et al.*, 2007; *Bibring et al.*, 2004a; *Brown et al.*, 2004; *Carlson et al.*, 1992]. These tasks are carried out through spectral analysis of solar light reflected by the material forming the top few millimeters or centimeters of the ground. Physical properties of the surface, such as chemical composition, granularity or texture are some of the most important parameters that characterize the morphology of spectra. Modeling the direct link between these parameters and observable spectra is called the forward problem. It can be evaluated numerically by radiative transfer models, simulating the propagation of solar light through the atmosphere and reflected back to the sensor [*Douté et al.*, 2007b; *Hapke*, 2002; *Shkuratov et al.*, 1999; *Douté and Schmitt*, 1998; *Hapke*, 1993]. Such models allow the simulation of spectra from given values of the model parameters. Conversely, deducing the physical model parameters from the observed spectra is called an inverse problem. Since it generally cannot be solved analytically, the use of optimization or statistical methods is necessary. Solving inverse problems requires an adequate understanding of the fundamental physics, so that a relation $x = G(y)$ may be specified between the spectra x and the parameters y. Given G, different methods can be used to deduce the parameters y from the observation x. Current solutions to the inverse problem can be divided into three main categories (for further details and comparisons, see *Kimes et al.* [2000] and *Pragnère et al.* [1999]).

[1] MISTIS, INRIA Rhône-Alpes, Saint Ismier, France.
[2] Laboratoire de Planétologie de Grenoble, Saint Martin-d'Hères, France.

0148-0227/09/2008JE003171

1.1. Optimization Algorithms

[3] These methods minimize an objective function that expresses the quality of the estimations, and include numerical optimization techniques such as Powell's method, Simplex method and the quasi-Newton method. Estimation can be unstable since inverse problems are often ill posed (solutions are not unique, and a small change in the data can lead to large differences in the estimations). A probabilistic formalism can be used to regularize (prevent overfitting) inverse problems by introducing a prior distribution on model parameters [*Aster et al.*, 2005; *Tarantola*, 2005]. These approaches are computationally expensive since they independently invert new spectra. Therefore, they cannot be used to invert an image with several hundred thousand pixels. Moreover, they can sometimes fall into local minima if the objective function is not convex.

1.2. Lookup Table/*k*-Nearest Neighbors Approach

[4] This methodology is currently used by physicists to study planetary bodies [*Carlson et al.*, 2005; *Philpot et al.*, 2004; *Weiss et al.*, 2000; *Douté et al.*, 2001]. The previous heavy runtime computation is replaced by a simpler lookup operation. A large database (lookup table (LUT)) is generated by radiative transfer calculations for many parameter values. To invert an hyperspectral image, the pixel's spectrum is then compared with the LUT spectra in order to find the best match (the nearest neighbor), according to an objective function minimization. Parameters are then deduced from this best match. The speed gain is significant in comparison to traditional optimization methods, since retrieving a value from memory is often faster than undergoing an expensive computation. The main disadvantages of this approach are the multiplicity of solutions and their instability [*Bernard-Michel et al.*, 2007].

1.3. Training Approaches

[5] They have been recently considered in the study of terrestrial vegetation [*Combal et al.*, 2002; *Durbha et al.*, 2007; *Pragnère et al.*, 1999]. A functional relationship

$$y = F(x) \tag{1}$$

between spectra and parameters is assumed. This relationship corresponds to the inverse of the physical model G in the forward problem. The idea is to use a LUT to estimate the underlying mathematical relationship F. This relationship then allow us to estimate the parameters of new spectra. The advantage of such a training approach is that, once the relationship has been established, it can be used for very large sets and for all new images with the same physical model. Among training approaches, neural networks [*Hastie et al.*, 2003, chapter 11] or support vector machines (SVM) [*Hastie et al.*, 2003, chapter 12] seem promising but the underlying learning process remains time consuming [*Combal et al.*, 2002; *Durbha et al.*, 2007; *Pragnère et al.*, 1999].

[6] Hyperspectral images on planets must be inverted with the following constraints: (1) Working with large data sets and various models require fast methodologies. (2) When dealing with very high dimensional data, one is faced with the "curse of dimensionality;" that is, the complexity of the analysis increases with the dimension of the data. (3) Observed spectra always contain some noise.

[7] In this paper, a new training approach is proposed: The Gaussian regularized sliced inverse regression (GRSIR) [*Bernard-Michel et al.*, 2009]. It is based on a dimension reduction technique first proposed by *Li* [1991] and similar to partial least squares regression (PLS) [*Hastie et al.*, 2003, chapter 3]. Dimension reduction techniques exploit the strong correlation among spectels in a spectrum. That correlation induces redundancy of information: few variables may explain the data. Dimension reduction techniques aim at finding the set of linear combination of the original observable best explaining the data. GRSIR has the advantage of being fast, stable, statistically and physically interpretable, and can also help to select an appropriate lookup table for inversion. This approach is validated using test data, compared with the *k*-Nearest Neighbors Approach (*k*-NN), PLS and SVM approaches, and then applied to Mars spectra.

[8] In section 2, real and simulated data sets are presented, then the principle of GRSIR is recalled in section 3. The choice of an appropriate LUT is discussed in section 4. Experimental results are presented on simulated data sets in section 5 and on real Mars images in section 6. Conclusions are drawn in section 7.

2. Data

[9] The data sets used in sections 2.1 and 2.2 can be divided in three categories: The hyperspectral images observed on Mars, a LUT simulated by radiative transfer algorithms according to some physical model of the icy surfaces, and test data in order to quantify the estimations. The physical model has been crafted guided by a preliminary analysis of these images. All data sets consist of some spectra (X, x_i, x_i^T for Mars, LUT, and test data, respectively). Each spectrum consists of a fixed number of wavelengths (d). The corresponding parameters (p in number) are denoted Y, y_i, and y_i^T. The index i denotes a particular spectrum or parameter combination in each set.

2.1. Hyperspectral Images From Mars

[10] The data sets were collected by the imaging spectrometer OMEGA (Observatoire pour la Minéralogie, l'Eau, la Glace et l'Activité) [*Bibring et al.*, 2004a]. OMEGA is one of the seven scientific instruments aboard the European spacecraft Mars Express mission, sent to orbit Mars in 2003. It was developed by IAS and LESIA (Observatoire de Paris) with the support of CNES, and with the participation of IFSI (Italy) and IKI (Russia). This visible and infrared instrument can scan most of Mars from orbit in order to observe gas and dust in the atmosphere and look for signs of specific materials such as silicates, carbonates and ice at the surface. It records the visible and infrared light reflected from the planet in the 0.5–5.2 micron wavelength range and with a ground resolution varying from 350 m to 10 km. Three OMEGA hyperspectral images acquired during orbits 41, 61 and 103 will be used. They cover the high southern latitudes of Mars. The spatial resolution is approximately 2 km per pixel and 184 wavelengths have been considered in the range 0.95–4.15 (i.e. $d = 184$). We refer the reader to *Douté et al.* [2007a] (section 2.1, Table 1, and Figure 1) for more information about the images. For each spectrum of

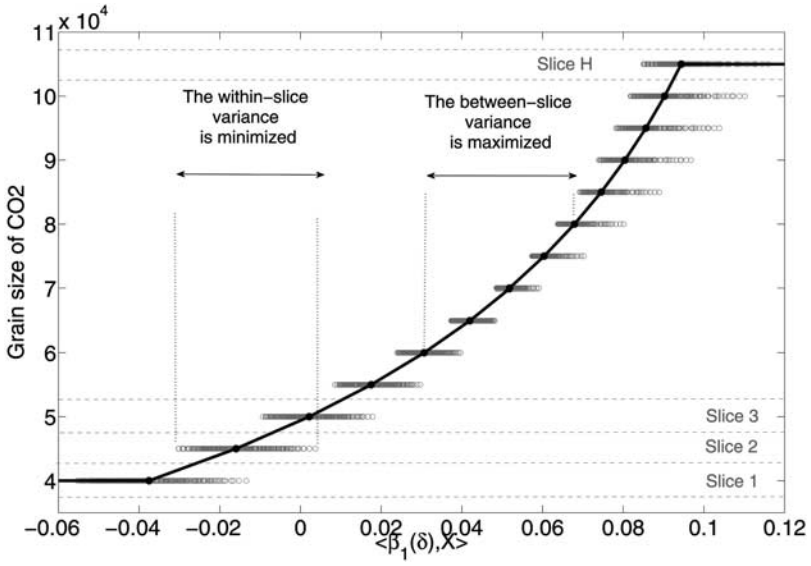

Figure 1. Functional relationship between reduced spectra on the first GRSIR axis and the grain size of CO_2 ice (in microns). This graphic illustrates the GRSIR methodology showing that the relationship is the best when the within-slice variance is minimized or equivalently when the between-slice variance is maximized.

the image, the atmospheric gaseous contribution has been removed [*Douté et al.*, 2007b]. After a first analysis, these OMEGA observations revealed that the south polar region of Mars exhibits mainly water ice, carbon dioxide ice and dust at the surface [*Bibring et al.*, 2004b]. The bright permanent polar cap has been mapped by a classification method based on wavelets [*Schmidt et al.*, 2007]. For each image, this area dominated by CO_2 ice signatures displays about 10,000 to 20,000 spectra. The latter are also slightly contaminated by the contribution of dust and water ice. Among the possible coexistence modes of the latter components, a granular mixture of H_2O ice, CO_2 ice and dust is the most appropriate to reproduce the morphology of the spectra [*Douté et al.*, 2007a]. This conclusion is based on numerical experiments that aimed at reproducing the spectra by different surface reflectance models. The selected model for the polar cap considers the intimate mixture of H_2O ice, CO_2 ice and dust as an optically thick parallel layer without substantial roughness. The transfer of solar photons through such a material is calculated by a modified version of the Hapke semiempirical formulation [*Hapke*, 2002; *Douté and Schmitt*, 1998; *Hapke*, 1993].

2.2. Lookup Table

[11] The physical model of the permanent polar cap implies five spatially varying parameters (i.e. $p = 5$): the grain size of water and CO_2 ice, the proportion of water ice, CO_2 ice, and dust. The proportions are the bulk mass fractions of the previous compounds and are normalized to sum to one. The grain sizes express the mean free path between two optical interfaces consecutively visited by photons in the material, i.e., the effective mean diameter of the water and CO_2 grains [*Hapke*, 1993]. The other parameters involved in the physical model, such as the incidence and emergence angles or the grain size of dust have been fixed to a constant. Since *a priori* knowledge on the parameters range is unavailable, the simulation of a large LUT is necessary. Details of the sampling strategy are provided in Table 1. The notation used in this article is as follows: n is the number of simulated spectra ($n = 31500$), $x_i \in \mathbb{R}^{184}$ denotes a spectrum from the LUT and $y_i \in \mathbb{R}^5$ its associated parameters.

2.3. Test Data

[12] For validation and comparison, the use of a test data set (Tdata) is required, i.e., a collection of spectra for which we have an unquestionable estimation of the physical parameters. Since no ground truth is currently available for the physical properties of Mars polar regions, we can only rely on synthetic data. The same physical model is used to simulate the LUT and Tdata. The range of variation for the parameter is detailed in Table 1. The spectra are computed using given combinations of the five parameters. After inversion, which is performed for each parameter individually, we quantify how close we retrieve the original set of 5 values for a given spectrum. To emulate real data, a centered multi-Gaussian noise of dimension 184 is added to all the spectra of the test data set. The covariance matrix is determined experimentally from a small, spatially homogeneous, portion of the real image. Assuming that much of the variability comes from the noise, the latter is then evaluated using statistics based on a shift difference on the selected portion. As in section 2.2, n_T is the number of simulated test

Table 1. Sampling Strategy for the Simulation of the Lookup Table[a]

	Lookup Table		
Parameters	Range	Number of Distinct Values	Test Data Range
Proportion of water	[0.0001 0.0029]	15	[0.0006 0.002]
Proportion of CO_2	[0.9942 0.9998]	29	[0.996 0.9988]
Proportion of dust	[0.0001 0.0029]	15	[0.0006 0.002]
Grain size of water	[50 450]	5	[100 400]
Grain size of CO_2	[30000 165000]	28	[40000 105000]

[a]The range of variation is given for each varying parameter as well as the number of distinct values simulated. The increment between two values is constant.

spectra (n_T = 3500), x_i^{Tdata} is a spectrum from Tdata and y_i^{Tdata} its associated parameters.

3. Proposed Approach

[13] Our goal is to estimate the functional relationship F between the spectra $x \in \mathbb{R}^d$ and each physical parameter $y^{(j)} = F(x) \in \mathbb{R}$ with $j \in \{1, \ldots, p\}$. In this work, each parameter is studied individually, therefore $p = 1$ and j will be omitted for the sake of simplicity. The originality of the methodology is to split the difficult problem of learning a d-variate function into two subproblems that can be easily solved. First, a dimension reduction technique is applied (section 3.1). Then, estimation is performed in the lower dimensional subspace (section 3.2).

3.1. Dimension Reduction Step: Gaussian Regularized Sliced Inverse Regression

[14] Dimension reduction methods rely on the assumption that the predictor x can be replaced, without loss of information, by its projection onto a subspace of smaller dimension L, called the effective dimension reduction space (EDR). The basis of the subspace is denoted $\beta_1, \ldots, \beta_L$ and the functional relationship $y = F(x)$ can be rewritten as $y = f(\langle\beta_1, x\rangle, \ldots, \langle\beta_L, x\rangle)$, where f is now a L-variate function and $\langle,\rangle$ the dot product. In most applications, L is smaller than 3 making the estimation of f tractable.

[15] Principal Component Analysis (PCA) is a classical approach to reduce the dimension [*Hastie et al.*, 2003, chapter 14]. The basic concept of PCA is to define the orthogonal projection of the spectra onto a lower dimensional linear space such that the total variance of the projected spectra is maximized. It amounts to diagonalize the spectra covariance matrix (the transpose vector operator is noted $()^t$)

$$\Sigma = \frac{1}{n}\sum_{i=1}^{n}(x_i - \bar{x})(x_i - \bar{x})^t \text{ where } \bar{x} = \frac{1}{n}\sum_{i=1}^{n} x_i \qquad (2)$$

or equivalently to calculation of the eigenvectors of Σ. However, in regression problems PCA is generally not satisfactory since only the explanatory variable x is considered while the dependent variable y is not taken into account. Specific dimension reduction techniques have been developed for regression problems, such as PLS and sliced inverse regression (SIR) [*Li*, 1991]. SIR consists of sorting the parameter values in increasing order and dividing them into H nonoverlapping slices S_h, $h \in \{1, \ldots, H\}$. For each slice S_h, a mean spectrum m_h is calculated as the mean value of the parameter values that are varying in the slice. The orthogonal projection of the mean spectra onto a lower dimensional linear space is defined so that the variance of the projected mean spectra is maximized under the constraint that the total projected variance is one. This is equivalent to diagonalization of $\Sigma^{-1}\Gamma$, where Γ is the mean spectra covariance matrix given in equation (3). The SIR principle is illustrated in Figure 1.

[16] Since inverse problems are generally ill posed [*Aster et al.*, 2005; *Tarantola*, 2005], Σ is ill conditioned, making its inversion difficult. To solve this problem, it is proposed to compute a GRSIR. Theoretical foundations can be found by *Bernard-Michel et al.* [2009]. The concept of this method is to include some prior information on the projections in order to dampen the effect of noise in the input data. The ill-posed problem is then replaced by a slightly perturbed well-posed problem that depends on a regularization parameter $\delta > 0$. Therefore, GRSIR computes the L eigenvectors corresponding to the L largest eigenvalues of $(\Sigma^2 + \delta I_p)^{-1}\Sigma\Gamma$ where I_p is the $d \times d$ identity matrix. In practice, GRSIR then requires the three following computational steps:

[17] 1. Choose δ and sort y_i into increasing order and divide into H nonoverlapping slices S_h, $h = 1, \ldots, H$. If the LUT has been simulated for random values of Y, then slices are chosen such that each slice contains the same number of observations. If the LUT has been simulated for a fixed number of distinct parameters, the slices are chosen to coincide with these discrete values.

[18] 2. Compute the "between-slices" covariance matrix of the means:

$$\Gamma = \sum_{h=1}^{H}\frac{n_h}{n}(\bar{x}_h - \bar{x})(\bar{x}_h - \bar{x})^t \text{ with } \bar{x}_h = \frac{1}{n_h}\sum_{x_i \in S_h} x_i \qquad (3)$$

where n_h denotes the number of observations in the slice S_h.

[19] 3. Estimate the GRSIR axes $\beta_1(\delta), \ldots, \beta_L(\delta)$ by computing the eigenvectors of $(\Sigma^2 + \delta I_p)^{-1}\Sigma\Gamma$. The first GRSIR axis, $\beta_1(\delta)$, is determined by the eigenvector corresponding to the largest eigenvalue, the second GRSIR axis, $\beta_2(\delta)$, is determined by the eigenvector corresponding to the second largest eigenvalue, and so on.

[20] In section 5.4, a criterion to choose the dimension L is given. Interestingly, the first axis can be viewed as a weighted function of the wavelengths, giving some knowledge about the wavelengths that carry information on the parameter (section 5.5). The projections of the spectra on the axis $\beta_1(\delta)$ is termed "reduced spectra".

3.2. Estimation of the Functional Relationship

[21] Once the spectra have been reduced, the relationship f has to be estimated. In the proposed approach, a piecewise linear interpolation is performed on the set of data points $(\bar{x}_h^{proj}, \bar{y}_h)$, $h = 1, \ldots, H$, where $\bar{x}_h^{proj} = \langle\bar{x}_h, \beta_1(\delta)\rangle$ denotes the projection of the mean spectra for slice S_h and $\bar{y}_h = \frac{1}{n_h}\sum_{y_i \in S_h} y_i$ denotes the average parameter value for slice S_h.

[22] For each new spectrum x with a projection $x^{proj} = \langle\beta_1(\delta), x\rangle$, the estimated parameter value $\hat{y}$ is then given by a piecewise linear regression:

$$\hat{y} = \begin{cases} \bar{y}_1 & \text{if } x^{proj} \in]-\infty, \bar{x}_1^{proj}] \\ \bar{y}_h + \left(x^{proj} - \bar{x}_h^{proj}\right)\left(\dfrac{\bar{y}_{h+1} - \bar{y}_h}{\bar{x}_{h+1}^{proj} - \bar{x}_h^{proj}}\right) & \text{if } x^{proj} \in]\bar{x}_h^{proj}, \bar{x}_{h+1}^{proj}],\ h = 1, \ldots, H-1 \\ \bar{y}_H & \text{if } x^{proj} \in]\bar{x}_H^{proj}, +\infty[\end{cases} \qquad (4)$$

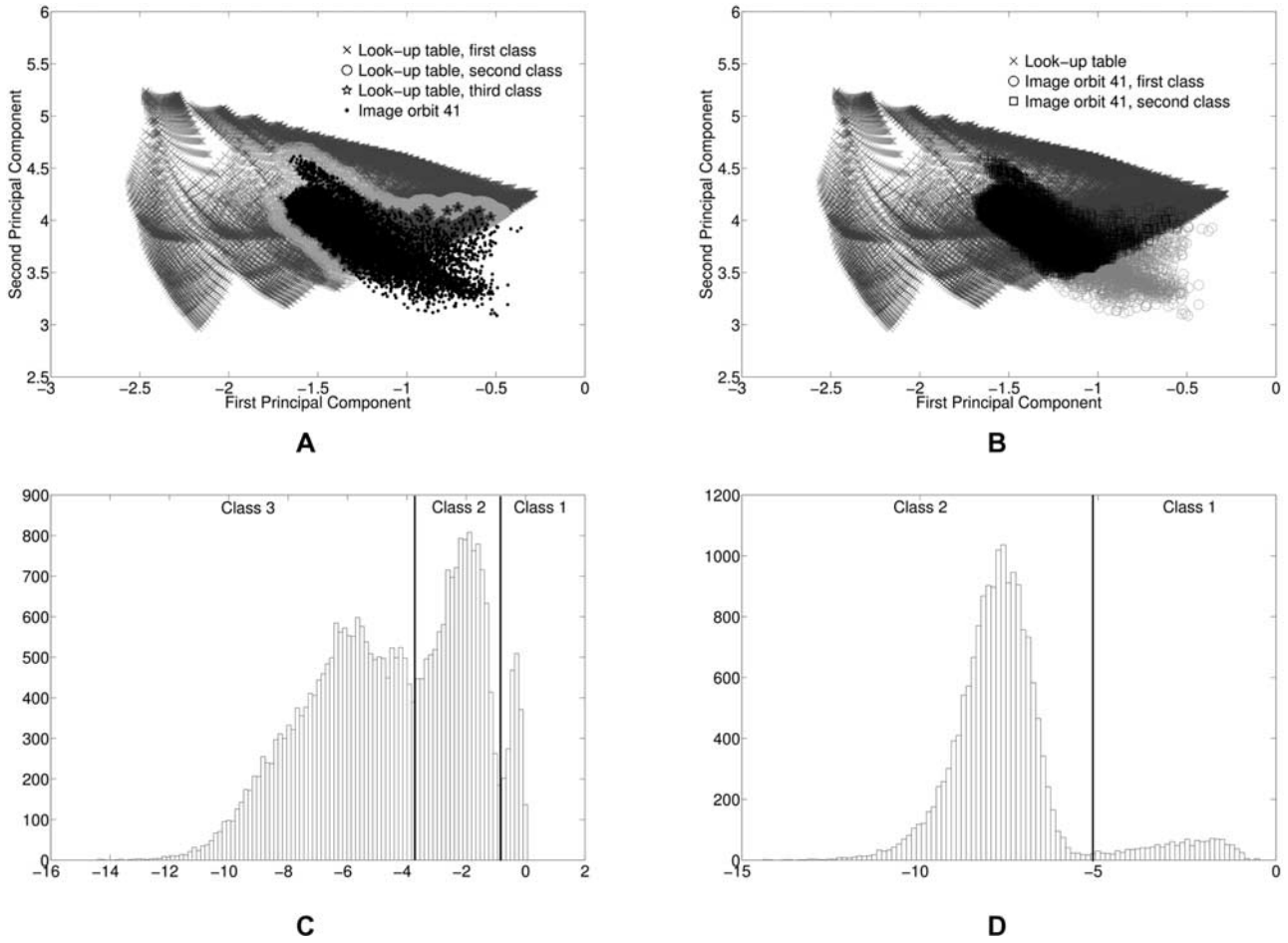

Figure 2. Selection of the useful spectra in the lookup table and of the invertible spectra in the observed data. (a) Selection of a lookup table. Projections of the observed spectra from orbit 41 and the lookup table on the two first PCA axes (PCA applied to the lookup table spectra). Three classes are identified. The third class is the retained lookup table. (b) Selection of invertible spectra in the image from orbit 41. The second class is retained for inversion. (c) Histogram of the distances between each spectrum of the lookup table and its nearest neighbor in the image from orbit 41. (d) Histogram of the distances between each spectrum of the image from orbit 41 and its nearest neighbor in the selected sublookup table.

An example of the application of GRSIR to the LUT is given in Figure 1. It shows the relationship between reduced spectra and the grain size of CO_2 ice and its estimation by a piecewise linear interpolation.

4. Choice of the Lookup Table

[23] In the simulated LUT, many spectra could be superfluous to the proper estimation of the parameters. For instance, considering Tdata, spectra with parameter values not included in the Tdata's parameter range should be removed from the LUT. Better estimations can be obtained with the reduced LUT [*Bernard-Michel et al.*, 2007]. The difficulty is that, in practical cases, the range of variation of the parameters is unknown. A good strategy is to assumed a large LUT and to reduce it after the first estimation. However, the effectiveness of this technique in practical situations depends strongly on the quality of the first estimation.

[24] In this paper, another approach is proposed that makes use of PCA to visualize the adequacy of the chosen LUT for a given set of observed spectra. The parameters of the observed spectra can be estimated only if their projections onto the first m PCA axes (deduced from the application of PCA to the LUT) coincide with the projection of the LUT itself. Conversely, to select the most appropriate spectra from the LUT for inversion, the strategy is to retain spectra from the LUT whose projections onto the PCA axes are close to projections of the spectra from the observed image (see Figure 2a). In the space spanned by the first m PCA axes, the distance between each projected LUT spectrum and its nearest neighbor from the projected spectra is computed. The histogram of these distances is considered as a mixture of n_C Gaussian distribution $\mathcal{N}(\mu_c, \Sigma_c)$ characterized by the proportions of the mixture π_c, $c \in \{1, \ldots, n_C\}$, the expectation μ_c and the covariance matrix Σ_c of each class c, $c \in \{1, \ldots, n_C\}$. The number of classes is chosen by the user, and the parameters can be estimated by the Expectation-Maximization algorithm (EM) after a random or a K-means initialization (for further details about mixture models and EM, see sections 6.8 and 8.5 of *Hastie et al.* [2003]). The algorithm is a simple iterative optimization process for computing the maximum likelihood estimate of

the parameters. One can then calculate and maximize the posterior probability that a spectrum belongs to a particular class by observing the aforementioned distances. This leads to a classification of the spectra into n_C classes. An example is given in Figure 2c with the image observed from orbit 41. The histogram allows us to distinguish 3 classes. The third class corresponds to spectra that belongs to both LUT and observed data.

[25] Note that in Figure 2b some of the observed spectra are outside the projected LUT. Since the chosen physical model is not relevant to them, these spectra are removed from the observed data. Hence, in the PCA space, the histogram of the distance of each observed spectrum with its nearest neighbor in the selected sub-LUT facilitates the distinction of two classes: The invertible spectra and the non invertible ones (Figure 2d). The non invertible spectra from orbit 41 correspond to pixels at the boundary of the CO_2 bright area and thus to pixels with a linear geographical mixture of terrains. Thus, the physical model used to simulate the data is not valid. Other examples can be found in the work of *Bernard-Michel et al.* [2007]. Experimental results in section 5.6 show that estimations are more accurate when applying such a selection.

5. Analyzing Results on Simulations

[26] In this section, the competing methods are first presented. Then, the validation criteria and the parameters selection are detailed. Finally, results on simulated data sets are given.

5.1. Competing Methods

5.1.1. The *k*-NN

[27] From the LUT one finds the k nearest spectra and fixes the estimated y as the mean parameter value of k nearest spectra parameter. The distance between two spectra is taken as the Euclidean distance: $\|X - x_i\|^2$, where X is a spectrum from the image and x_i a spectrum from the LUT. In the experiments, k is fixed to one, so only one neighbor is used for the estimation.

5.1.2. Partial Least Squares Regression

[28] The PLS method is closely related to PCA (orthogonal projection onto lower dimensional space) and GRSIR (y is accounted for). PLS searches for the projection of the explanatory variable x onto a lower dimensional space that maximizes the covariance between x and y: $\max_{\beta} \mathrm{cov}^2(y, \langle \beta, x \rangle)$. PLS is parametrized by the size L of the subspace spanned by β. The regression in the subspace is necessarily linear and may limit the efficiency of the method if a non linear relationship exists between x and y.

5.1.3. Support Vector Machines Regression

[29] SVM approximates the functional F: $y = F(x)$ using a solution of the form $F(x) = \sum_{i=1}^{n} \alpha_i K(x, x_i) + b$, where x_i are samples from the training set, K a kernel function and $((\alpha_i)_{i=1}^n, b)$ are the parameters of F which are estimated during the training process [*Scholkopf and Smola*, 2002]. The kernel K is used to produce a nonlinear function. One widely used kernel is the Gaussian Kernel: $K(x_i, x_j) = \exp(-\gamma \|x_i - x_j\|^2)$. The SVM training entails minimization of $[\frac{1}{n}\sum_{i=1}^{n} l(F(x_i), y_i) + \lambda \|F\|^2]$ with respect to $((\alpha_i)_{i=1}^n, b)$, and with $l(F(x), y) = 0$ if $|F(x) - y| \leq \epsilon$ and $|F(x) - y| - \epsilon$ otherwise. Prior to running the algorithm, the following parameters need to be fitted: ϵ which controls the resolution of the estimation, λ which controls the smoothness of the solution and the kernel parameters (γ for the Gaussian kernel). The SVM have been implemented using the library LIBSVM written in C++ through its matlab interface (C.-C. Chang and C.-J. Lin, LIBSVM: A library for support vector machines, software available at http://www.csie.ntu.edu.tw/~cjlin/libsvm, 2001).

5.2. Validation Criteria

[30] To assess the relevance of GRSIR methodology, two aspects of the estimation were investigated: The accuracy of the estimates and the quality of the relationship between the reduced spectra and the parameters. To this end, two validation criteria were used

[31] 1. The normalized root-mean-square errors (NRMSE):

$$NRMSE = \sqrt{\frac{\frac{1}{n_T}\sum_{i=1}^{n_T}\left(\hat{y}_i^{Tdata} - y_i^{Tdata}\right)^2}{\frac{1}{n_T}\sum_{i=1}^{n_T}\left(y_i^{Tdata} - \bar{y}^{Tdata}\right)^2}} \quad \text{with } \bar{y}^{Tdata} = \frac{1}{n_T}\sum_{i=1}^{n_T} y_i^{Tdata} \tag{5}$$

The NRMSE quantifies the difference between the estimations $\hat{y}_i^{Tdata}$ and the real values y_i^{Tdata}. This measure is normalized by the standard deviation enabling direct comparisons between estimations of parameters with different range of variations. The closer NRMSE is to zero, the more accurate are the predicted values.

[32] 2. The SIR Criterion (SIRC)

$$SIRC(\ell) = \frac{\beta_\ell(\delta)^t \Gamma \beta_\ell(\delta)}{\beta_\ell(\delta)^t \Sigma \beta_\ell(\delta)} \text{ with } \ell \in \{1, \ldots, L\} \tag{6}$$

The SIRC is the ratio between the "between-slices" variance $\beta_\ell(\delta)^t \Gamma \beta_\ell(\delta)$ of the projections of x_i on $\beta_\ell(\delta)$, and the total variance $\beta_\ell(\delta)^t \Sigma \beta_\ell(\delta)$ of these same projections. It quantifies the quality of the relationship between projected spectra and parameters. The closer SIRC is to 1, the better is the relationship.

5.3. Choice of the Parameters

[33] For GRSIR, the quality of the estimation $\hat{y}_i^{Tdata}$ depends on a regularization parameter δ (see section 3.1). When δ increases, the functional relationship between projected spectra and parameters gets worse and consequently estimation errors increase. On the contrary, if δ is too small, then the estimation errors are considerable in the presence of noise because the problem is ill posed. So, the choice of δ dictates to a compromise between improving the functional relationship and increasing estimation accuracies by regularization. In this article, δ is chosen for each parameter individually, the NRMSE criterion calculated between the parameter values from a validation data and their estimations is minimized. The validation data is the lookup table itself, perturbed by multi-Gaussian noise representative of that affecting the OMEGA hyperspectral images (see section 2.3). It is noted that if there is no noise in the data, i.e., if the observed data exactly corresponds to spectra that could be simulated by radiative transfer model, then no regularization is required, and minimizing the NRMSE criterion for GRSIR yields a value δ close to zero.

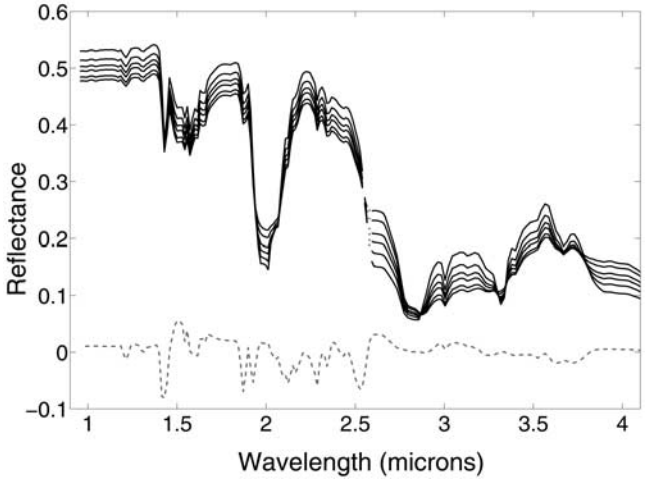

Figure 3. Solid line is series of spectra extracted from the lookup table for CO_2 ice grain size varying between 30 and 165 millimeters, the other parameters being kept constant at mean values. Dashed-dotted line is component wise multiplication between GRSIR axis for the grain size of CO_2 ice and a representative spectrum (see section 5.5).

[34] For k-NN, since k is fixed to one, no parameter tuning is required. For PLS, the dimension L of the subspace is chosen to minimize the NRMSE on the validation set. For SVM, three parameters are fixed. ϵ is fixed to 0.01, while λ and γ are selected to minimize the NRMSE on the validation set. As it is typically done with SVM, the range of each component of Y has been stretched between 0 and 1 for the regression.

5.4. Choice of the EDR Dimension

[35] In order to choose the EDR dimension, the SIRC is calculated for each GRSIR axis $\beta_\ell(\delta)$. As ℓ increases, the SIRC decreases rapidly and is almost zero after a few iterations. For instance, when applying GRSIR to the LUT, the SIRC for the proportion of CO_2 ice on the first GRSIR axis is 0.985. It indicates that the relationship of interest is captured by the first axis. Calculated for the second axis, the SIRC drops to 0.1799 and then is close to zero for other axes. In this case, one can consider incorporating these axes in the regression step does not bring extra information and is unnecessary, and finally fixes the EDR dimension to one. Analyzing the SIRC over all parameters and two different physical models reveals that in most situations only one dimension is necessary to retrieve the model parameters. Hence, in this article L is fitted to one.

5.5. Analyzing the GRSIR Axis

[36] The spectral variability of the x_i constituting the LUT arises from a complex interplay of the different input parameters y_i of the model. In particular, two parameters can have a similar influence on the spectra for a certain range of values. Consequently, it is crucial to understand how the GRSIR method can untangle the dependencies in order to find an independent one-to-one functional relationship between spectra and parameters. Accordingly, we attempt to correlate each axis $\beta_1(\delta)$ (which is a vector of spectral weights) with the variability induced by the variation of the corresponding physical parameter. The other parameters are kept constant at mean values. The weights are individually applied to different levels of reflectance, depending on the associated wavelength, to calculate the reduced spectrum $\langle \beta_1(\delta),\ x_i \rangle$. Hence, we find it more illustrative to represent the component wise multiplication (wavelength by wavelength) of each axis with a representative spectrum. An illustration is given in Figure 3 for the grain size of CO_2 ice. Additionally we overplot in Figure 4 the absolute value of the axis (for the sake of clarity) for the proportions of water ice and dust and of the grain sizes of water and CO_2 ice. Our analysis shows that the axis for H_2O abundance, dust abundance, and grain size of CO_2 ice are quite similar. A strong weight is assigned to 1.43 micron wavelength (the bottom of a very reliable and narrow CO_2 ice absorption band) and, to a lesser extent, to the interval between 1.47 and 1.54 microns (H_2O ice feature), and wavelengths of 1.87 and 2.29 microns (weak CO_2 ice bands but very distinct). The three axes also show differences that allow differentiation between the functional relationships. A relatively strong weight at 2.38 microns on the right wing of the 2.34 micron band is a specificity of the proportion of water ice. The axis for the proportion of dust stresses very much the variation of the spectrum continuum around 1 micron and 1.77 micron that indeed strongly changes with dust concentration. No other parameter affects the continuum as much. The axis for the grain size of CO_2 ice maximizes the influence of the small plateau at 2.62 microns that varies very much with the latter parameter. The axis that is linked to H_2O grain size is unique in the fact that it emphasizes, on the one hand, the continuum level around 1 micron, but not around 1.75 microns and, on the other hand, the entire spectral range between 2.35 and 2.65 microns. The main conclusions that can be drawn from this study are that, at least for the model presented in this paper, the GRSIR method has the ability to find a unique set of wavelengths where the variability of the spectrum is the most pertinent (but not necessary the highest) for the evaluation of a given parameter. One must note that these key wavelengths not only fall on the bottom of specific absorption bands for both H_2O and CO_2 ices but also on specific parts of the continuum as well as on specific band wings.

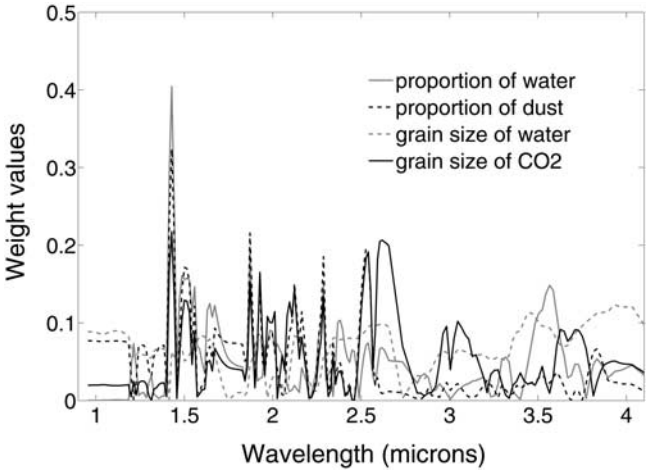

Figure 4. Absolute value of GRSIR weights versus wavelength for the proportions of water ice and dust and the grain sizes of water and CO_2 ices.

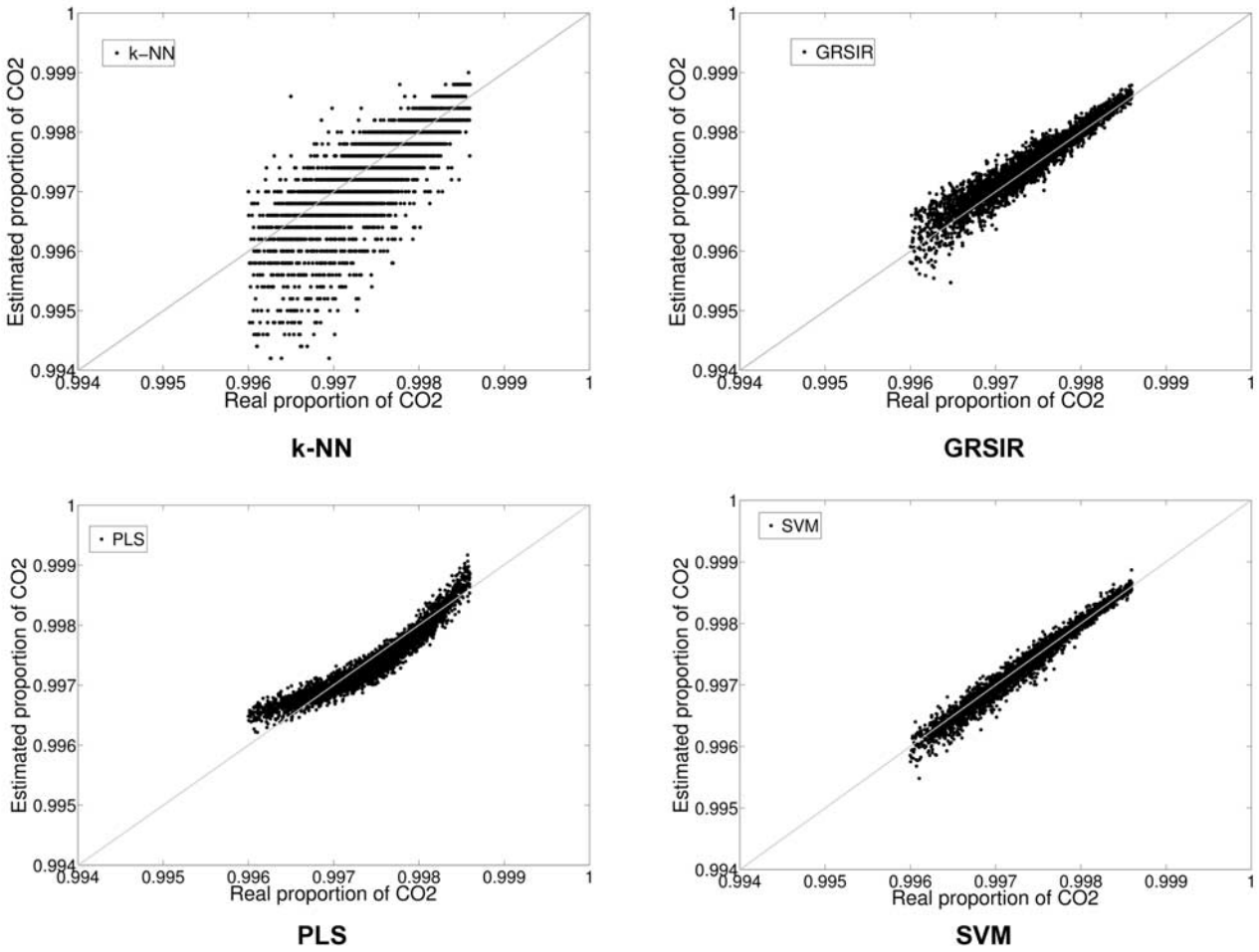

Figure 5. Scatterplots of estimated proportions of CO_2 ice by k-NN, GRSIR, PLS, and SVM (vertical axis) versus the proportion of CO_2 ice from the test data (horizontal axis).

5.6. Results

[37] In this section, the results obtained by inverting the test data set with the selected competing methods are compared in terms of the NRMSE and SIRC (Table 2), and also with scatterplots of input and estimated parameters (Figure 5). The scatterplots illustrate the absolute accuracy of a given method independently for each parameter while the NRMSE measure allows for comparative accuracy studies among parameters or between methods (GRSIR, PLS, etc.). Except for *k*-NN, a spectra selection in the lookup table was performed before applying the different algorithms, as mentioned in section 4.

[38] From Table 2, it is clear that the worst results are obtained with *k*-NN. GRSIR outperforms *k*-NN and PLS for most parameters. Problems with the estimation of the grain size of water ice may be due to the fact that not enough values are considered for simulations in the LUT (only 5). SVM provides the best estimation in terms of the NRMSE, but with a dramatic increase in processing time: Approximately 15 hours against about 1 minute versus *k*-NN or GRSIR.

Table 2. Validation Criteria Calculated on Tdata With GRSIR, *k*-NN, PLS, and SVM[a]

				GRSIR	
	k-NN NRMSE (%)	PLS NRMSE (%)	SVM NRMSE (%)	NRMSE (%)	SIRC (%)
Parameters					
Proportion of water	86	52	*17*	*40*	90
Proportion of CO_2	88	*56*	18	30	98
Proportion of dust	44	36	11	17	99
Grain size of water	43	44	17	54	84
Grain size of CO_2	53	47	14	22	95
CPU time	60s	181s	55,000s	58s	

[a]Note that the italicized values have been fixed such that the sum of the proportions is one. For *k*-NN inversion the LUT contains 31500 spectra. For other methods, the LUT after selection contains 15407 spectra. GRSIR, Gaussian regularized sliced inverse regression; *k*-NN, *k*-nearest neighbors approach; PLS, partial least squares regression; SVM, support vector machines, NRMSE, normalized root-mean-square errors.

Table 3. Validation Criteria Calculated on Tdata With GRSIR, PLS, and SVM[a]

	PLS NRMSE (%)	SVM NRMSE (%)	GRSIR NRMSE (%)	GRSIR SIRC (%)
Parameters				
Proportion of water	35	*18*	*27*	92
Proportion of CO_2	*32*	17	22	99
Proportion of dust	23	13	13	99
Grain size of water	45	23	39	92
Grain size of CO_2	28	15	19	98
CPU time	832s	2,750s	19s	

[a]The 3584 spectra that constitute the lookup table have been selected after a first inversion by GRSIR. Note that the italicized values have been fixed such that the sum of the proportions is one.

[39] Figure 5 shows the scatterplot of the estimated proportions of CO_2 ice with each method versus the real proportions. It appears that the range of the estimated proportions of CO_2 ice is much larger with *k*-NN than with GRSIR, PLS and SVM. PLS's scatter plot is slightly curved: PLS could not handle the non linear relationship between *x* and *y*, while GRSIR was able to model it. Scatterplots for other parameters appear in the work by *Bernard-Michel et al.* [2007].

[40] It is interesting to point out that a two stage inversion scheme can be built with GRSIR for increased performances. A first run of the method can determine the ranges of parameter variation for an observed image. Then, a more appropriate LUT can be built in the estimated ranges with a higher density of parameter values. Applying GRSIR in a second run with this new extracted LUT leads to more accurate estimations comparable to SVM, see Table 3. Finally, the SIRC, always close to 1, is very satisfying. Note that PLS benefits from the new LUT in terms of accuracy while the SVM does not. However, for the SVM, the processing time is decreased since the number of samples in the LUT is reduced.

6. Retrieval of the Physical Parameters for the South Polar Cap of Mars

[41] This section compares and discusses the first model inversions obtained by the different algorithms for hyperspectral images acquired by OMEGA during orbits 61, 103, and 41 (see section 2). The study of these images leads to

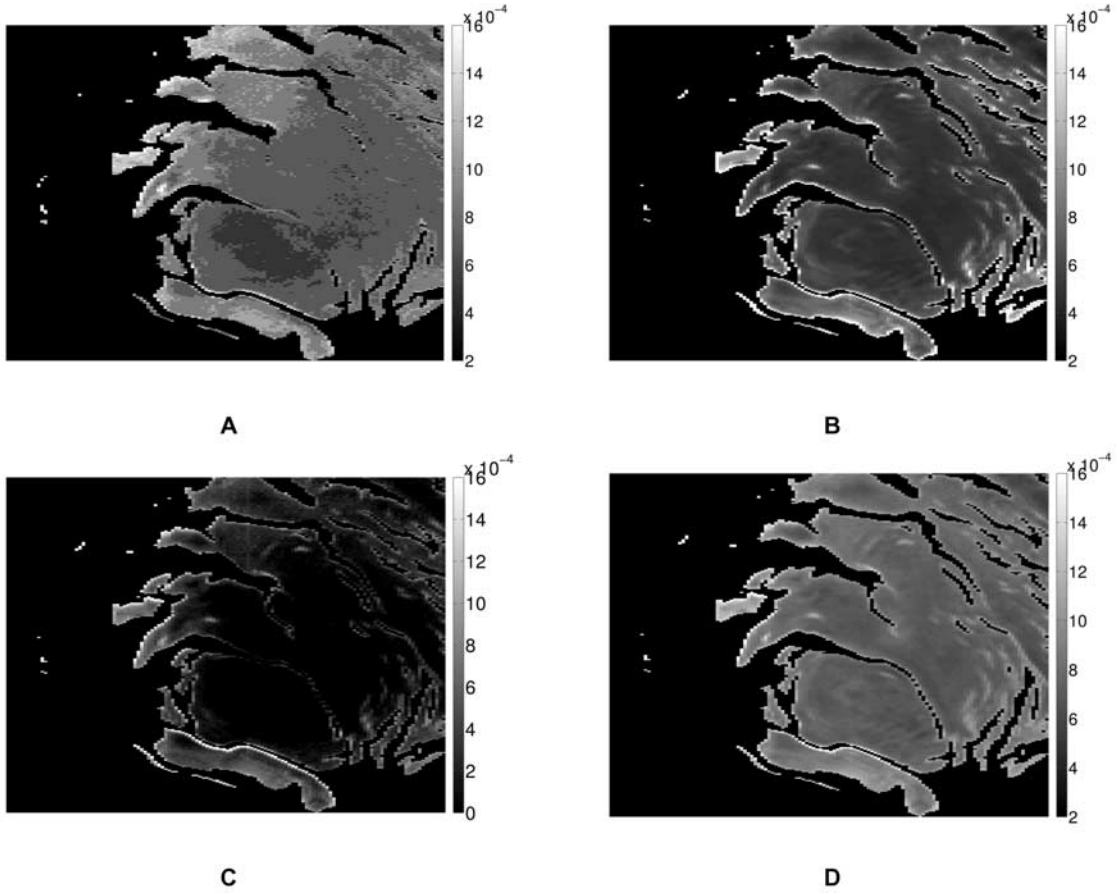

Figure 6. Proportion of dust estimated by (a) *k*-NN, (b) GRSIR, (c) PLS, and (d) SVM from the hyperspectral image observed from orbit 41.

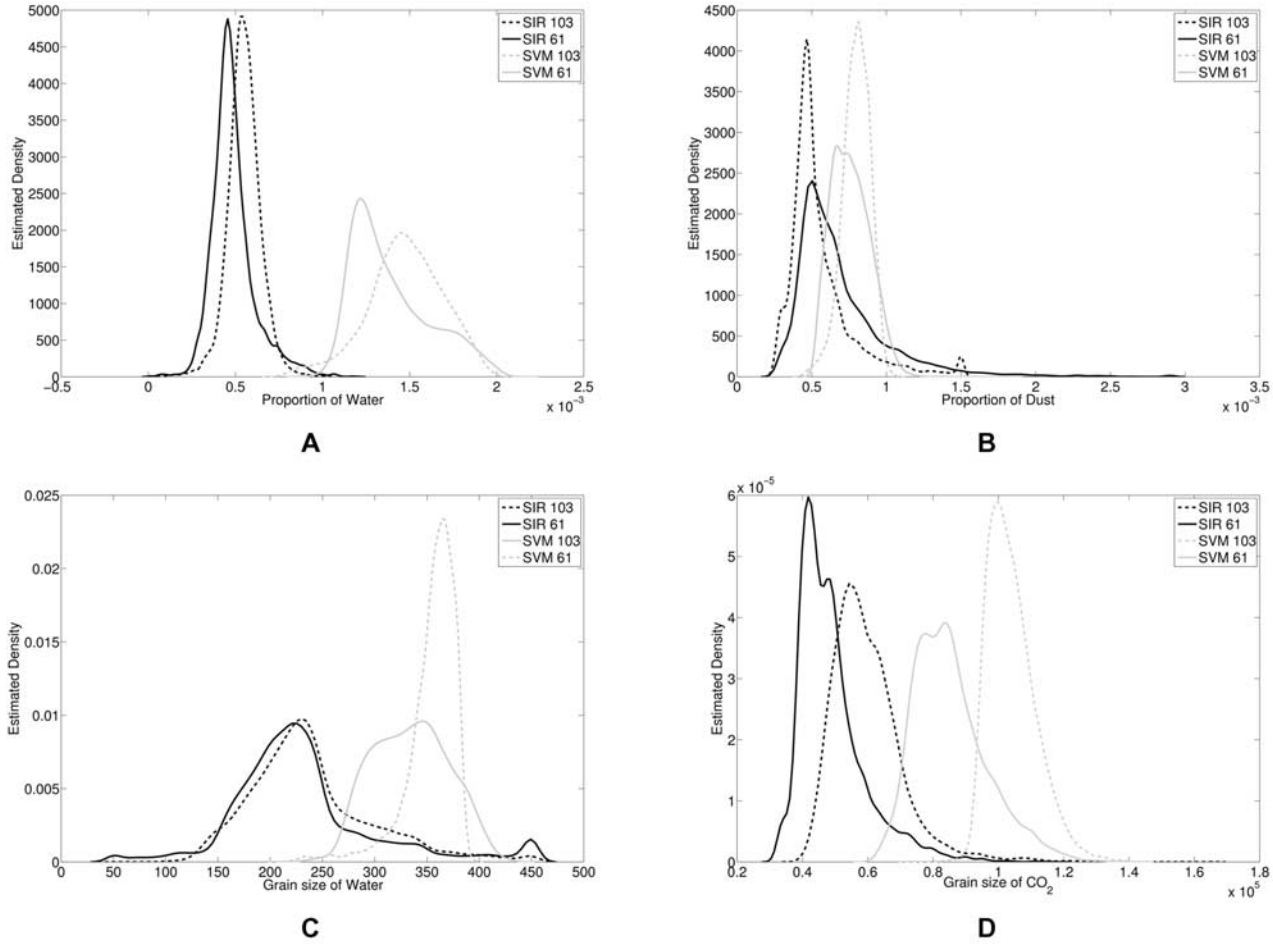

Figure 7. Distribution of values obtained for all parameters, respectively, by GRSIR and SVM for observations 61 and 103.

30 different maps. All the individual maps can be found in the work by *Bernard-Michel et al.* [2007]. For brevity, only some are reported in the article along with four global mosaics illustrating the absolute variations of water ice and dust proportions, as well as water and CO_2 ice grain size for the entire permanent bright polar cap.

6.1. Comparison Between Inversion Methods and Images

[42] The model inversion on the image observed from orbit 41 by GRSIR, PLS, SVM and *k*-NN shows that GRSIR and SVM give very smooth mappings for all sets of parameters. Figure 6 shows the proportion of dust estimated by the different algorithms on this portion of the polar cap. With *k*-NN, estimations assume 8 different values and seem to indicate that, at the very center of the bright cap, little dust is observed. The abundance of dust increases significantly with proximity to the boundaries. The estimated map with GRSIR is more detailed and leads to slightly different conclusions. In particular, the area presenting a low proportion of dust is more extended than with *k*-NN. Nevertheless if, globally, maps are much smoother and detailed with GRSIR, they never differ entirely from *k*-NN's. Some problems are encountered, with PLS: negative values are estimated, making the map difficult to interpret.

[43] Another interesting remark concerns the estimation of parameters in images 61 and 103 that represent approximately the same portion of the polar cap. The analysis should consequently give close estimations for each studied parameter regardless of the method. Figure 7 shows the distribution of the estimated proportion of water and dust and the distribution of the estimated grain size of water and CO_2 for both observations with GRSIR and SVM which are the two best choices (see section 5.6).

[44] First, we consider the evolution of these histograms between observations 61 and 103 for a given method. For CO_2 grain size and, to a lesser extent for H_2O grain size, a shift in the distribution of values can be noted that is increasing when using GRSIR, then SVM, and finally *k*-NN. The histograms of abundances for H_2O ice and dust are relatively stable between 61 and 103 with SVM and GRSIR. The abundance for CO_2 ice would present a similar behavior since it is fully constrained (sum of abundances equals 1). Observations 61 and 103 were acquired approximately 12 Mars days apart during a period of the year when the solar illumination was declining over the south pole. The conjugated effect of an increasingly grazing illumination over a slightly dusty atmosphere

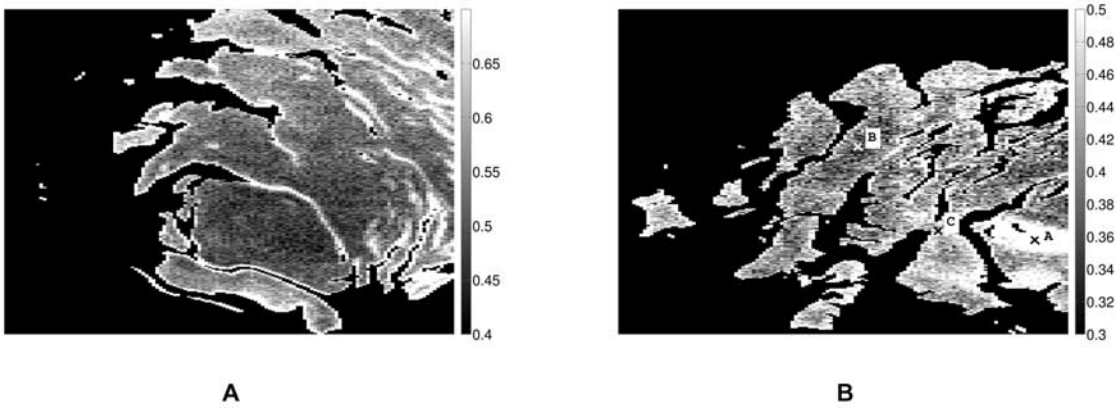

Figure 8. Cosines of the wavanglet angle between the observed spectra and a reference spectrum of Martian dust for the hyperspectral images acquired during (a) orbit 41 and (b) orbit 103.

(aerosol optical depth $\tau \approx 0.07$ at $\lambda \approx 2.65$ μm) [*Vincendon et al.*, 2008] diminishes the spectral contrast of the observations, i.e., the overall level of reflectance of the spectra and on the CO_2 ice bands intensity and shape. Although it is limited, the decrease of contrast may explain the moderate shift in the distribution of values between observations 61 and 103 for a given method.

[45] Second, we note that the distributions of parameter values obtained by SVM are always shifted compared to the distributions obtained by GRSIR for a given observation. The shift is always noticeable, sometimes considerable, and in addition systematically positive. Since our remote sensing problem is partly ill conditioned, a non regularized inversion method such as the *k*-NN is much more sensitive to noise than a regularized one such as the GRSIR or SVM. Even though regularization is thus applied to SVM, we note degraded performance when compared to GRSIR. For both methods, the estimation of the optimal value for the regularization parameter δ or λ is sensitive to the noise statistics applied to Tdata. In turn, this value determines the estimation of *Y*. As a consequence, uncertainties on the noise statistics propagate to bias on the estimation. We suspect that the choice of λ is less robust in the case of SVM than the choice of δ in the case of GRSIR.

6.2. Comparison With a Detection Method

[46] Finally, as an additional validation, the estimated parameter maps are compared with the wavanglet approach developed by *Schmidt et al.* [2007]. ''Wavanglet'' is a supervised automatic detection method that identifies in hyperspectral images spectral features and thus produces distribution maps of chemical compounds. It uses three steps: (1) Selection of a library composed of reference spectra (the signature of the compounds to be detected); (2) application of a Daubechies wavelet transform to referenced spectra and determination of the wavelet subspace that best separates all referenced spectra; (3) in this selected subspace, calculation of the spectral angle between each spectrum of an observation and a given reference spectrum. In particular, this angle called the wavanglet angle, allows to quantify in a relative sense the spatial variations of the different compound abundances at the surface. The cosine of the wavanglet angle between each spectrum of the images and a reference spectrum of Martian dust is presented Figure 8. The closer it is to one, the greater the dust proportion is. A similar map is observed for the water proportion. Globally, estimates of the latter quantities are more noisy with wavanglet than with GRSIR and *k*-NN, especially for the dust proportion but they generally are in agreement with some exceptions. For example, in the image observed during orbit 103, *k*-NN, SVM, PLS and wavanglet methodologies display an area with strong proportion of dust in Figure 8b (bottom right), that is absent with GRSIR. In order to check if this area really contains more dust than other areas, the spectrum denoted by A in Figure 8 is selected, corresponding to the greatest proportion of dust, and compared to two other spectra from the cap. The first spectrum (B) has been chosen in a pure CO_2 area with very few dust. The second one (C) has been chosen in a area containing dust. According to *k*-NN, SVM, PLS and wavanglet results, this area should however contain less dust than the area containing spectrum A. The spectra A, B, and C are presented in Figure 9. One can see that, as expected, the spectrum B is really different from the spectrum A. On the other hand, spectra A and C are really

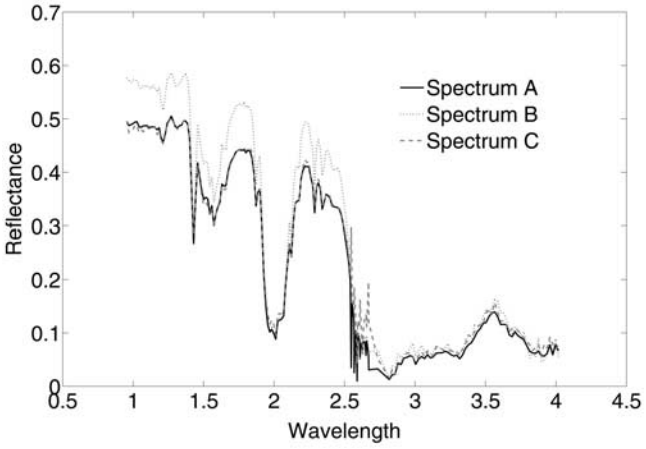

Figure 9. Spectra extracted from the locations labeled A, B, and C in the image 103 of Figure 8b.

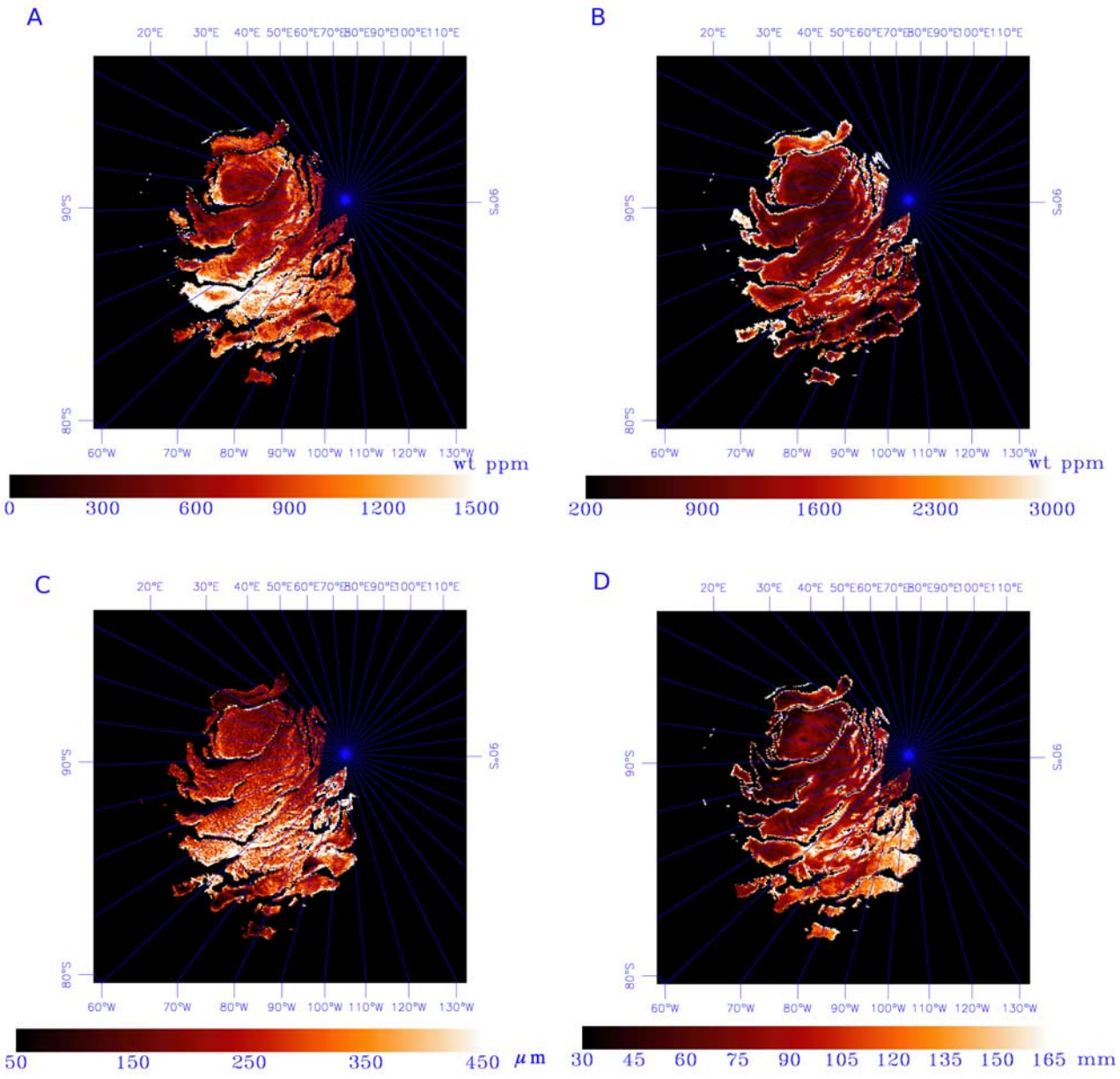

Figure 10. Global mosaics illustrating the absolute variations of (a) water ice and (b) dust proportions, as well as (c) water ice and (d) CO_2 ice grain sizes across the entire permanent bright polar cap. They are derived from individual parameter maps obtained by inversing OMEGA observations 41, 61, and 103 with GRSIR.

similar showing that the area of interest does not contain as much dust as the wavanglet methodology predicts. On the contrary, estimations given by GRSIR are more coherent with this spectral analysis.

6.3. Discussion of the Southern Permanent Cap Properties

[47] The parameter maps estimated by GRSIR are georeferenced using ancillary data provided by the OMEGA team and then are merged into global geographical mosaics. The latter covers the entire bright permanent polar cap (BPPC) with the exception of a limited area centered around (89°27′S, 34°58′W). We focus on the absolute variations of four unconstrained parameters: water ice and dust proportions, water and CO_2 ice grain size (Figure 10). The mosaics do show very few artificial discontinuities across the cap contrary to counterparts that we generated using parameter maps obtained by *k*-NN. This smoothness is an additional proof that GRSIR gives consistent results from observations acquired by OMEGA under different conditions. The different parameters do not show any obvious intercorrelation. Furthermore the mosaics provide a picture that is comptatible in its broad lines with the one drawn by *Douté et al.* [2007a]. These authors estimated trends of variations for water and dust contents in the CO_2 ice of the BPPC by combining classification techniques and selective physical modeling of individual representative spectra (see section 3.3 and Figure 13 of the latter paper). Mosaics of

Figure 10 provide a more detailed and sometimes different picture of these variations:

[48] 1. Dry ice completely dominates (≈99.55–99.95 wt%) the material forming the top few centimeters of the BPPC with dust and water only present as traces.

[49] 2. The water and dust contents increase, respectively, by a factor of ≈3 (300 to 1000 ppm) and ≈4 (280 to 1100 ppm).

[50] 3. The largest spatially coherent parts of the eastern BPPC constitute the most homogeneous terrains in terms of physical properties with moderate water and dust contents (≈350–450 ppm).

[51] 4. The purest dry ice (≈250–300 ppm of dust and water) can be mostly found within a region formed by a quite linear (in polar stereographic projection) but discontinuous segment of the BPPC extending from (84°S, 65°W) to (86°45′S, 96°W). These low concentrations of dust and water are conjugated with fine water ice grains (≈150 μm).

[52] 5. The largest amounts of H_2O ice can be found in a region extending between longitudes 50°W and 80°W northward from parallel 87°S.

[53] 6. The mean CO_2 grain size, around 5 cm on the average, undergoes noticeable variations (±50%) over the cap with a regional increase going from east to west.

[54] 7. It is substantially reduced (3.0–4.0 cm) compared to the typical situation in a shoe-like peninsula, (85°S,18°W) which is otherwise normal in H_2O and CO_2 contents.

[55] 8. The dry ice presents very few interfaces per unit length (mean free path of the order of 10–15 cm) for a region extending between longitude 80°W and 110°W northward from parallel 87°S. This advanced state of metamorphism (to the point where, likely, individual grains can no longer be distinguished) seems to be correlated to a lower contamination by dust (300–400 ppm) than the average.

[56] We do not discuss the planetary implications of these results since that will lead us farther than the scope of this paper. Furthermore interpretations and comparisons with other works that could be given are very similar to the ones that can be found in the work by *Douté et al.* [2007a].

7. Conclusion

[57] In this paper, a regularized version of Sliced Inverse Regression has been proposed to retrieve the physical parameters that best explain the spectra observed on Mars by the OMEGA imaging spectrometer. Results are promising:

[58] 1. On simulated data the estimations are accurate and most of the time better than the ones given by the *k*-NN algorithm or PLS and close to those given by SVM. If best results in terms of the NRMSE were obtained with SVM, the processing time with the latter one is 900 times more than GRISIR.

[59] 2. On a real data the maps are much smoother than with *k*-NN or PLS. They compare well with other approaches (spectral angles, classification techniques coupled with selective physical modeling) while giving more details. Moreover, the choice of the regularization parameter is more robust with GRSIR than with SVM, since the inversion of different hyperspectral images of the same portion of Mars surface but acquired at different times is more coherent with GRSIR. This leads to global mosaics showing very few artificial discontinuities across the cap contrary to what we produce with other methods.

[60] The main limitation of the proposed approach is that currently no uncertainties on the estimations are given when inverting a real image. Experimental uncertainties could be computed on the basis of simulations, but it supposes that the noise in the spectra has been well evaluated. If not, uncertainties will probably be underestimated. Some improvements could also be proposed to choose the regularization parameter and a more complete analysis of the influence of the noise in the GRSIR methodology would be interesting. Finally, the development of a multivariate regularized GRSIR under constraint is conceivable in order to estimate proportions simultaneously.

[61] **Acknowledgments.** The authors would like to thank the reviewers for their many helpful comments. They also appreciate the contribution of Senan Doyle to this paper. We thank the OMEGA team at IAS for support with sequencing and data downlink activities. This work is supported by a contract with CNES through its Groupe Système Solaire Program and by INRIA. It would not be possible also without the financial support of the Agence Nationale de la Recherche (French Research Agency) through its MDCO program (Masse de Données et Connaissances). The Vahiné project was selected in 2007 under the reference ANR-07-MDCO-013.

References

Aster, R., B. Borchers, and C. H. Thurber (2005), *Parameter Estimation and Inverse Problems*, Elsevier, Amsterdam.

Bernard-Michel, C., S. Douté, L. Gardes, and S. Girard (2007), Estimation of Mars surface physical properties from hyperspectral images using sliced inverse regression, *Tech. Rep. 00187444*, Inst. Natl. Rech. Inf. Autom., Rhône-Alpes, France.

Bernard-Michel, C., L. Gardes, and S. Girard (2009), Gaussian regularized sliced inverse regression, *Stat. Comput.*, *19*, 85–98, doi:10.1007/s11222-008-9073-z.

Bibring, J.-P., et al. (2004a), OMEGA: Observatoire pour la Minéralogie, l'Eau, les Glaces et l'Activité, in *Mars Express: The Scientific Payload*, *Eur. Space Agency Spec. Publ., ESA SP 1240*, 37–49.

Bibring, J.-P., et al. (2004b), Perennial water ice identified in the south polar cap of Mars, *Nature*, *428*, 627–630.

Brown, R. H., et al. (2004), The Cassini visual and infrared mapping spectrometer (Vims) investigation, *Space Sci. Rev.*, *115*, 111–168, doi:10.1007/s11214-004-1453-x.

Carlson, R. W., P. R. Weissman, W. D. Smythe, J. C. Mahoney, and NIMS Science and E. Teams (1992), Near infrared spectrometer experiment on Galileo, *Space Sci. Rev.*, *60*, 457–502.

Carlson, R. W., M. Anderson, R. Mehlman, and R. Johnson (2005), Distribution of hydrate on Europa: Further evidence for sulfuric acid hydrate, *Icarus*, *177*, 461–471.

Combal, B., F. Baret, M. Weiss, A. Trubuil, D. Macé, A. Pragnère, R. Myneni, Y. Knyazikhin, and L. Wang (2002), Retrieval of canopy biophysical variables from bidirectional reflectance using prior information to solve the ill-posed inverse problem, *Remote Sens. Environ.*, *84*, 1–15.

Douté, S., and B. Schmitt (1998), A multilayer bidirectional reflectance model for the analysis of planetary surface hyperspectral images at visible and near-infrared wavelengths, *J. Geophys. Res.*, *103*, 31,367–31,390.

Douté, S., B. Schmitt, R. M. C. Lopes-Gautier, R. W. Carlson, L. Soderblom, and J. Shirley (2001), Mapping SO_2 frost on Io by the modeling of NIMS hyperspectral images, *Icarus*, *149*, 107–132.

Douté, S., B. Schmitt, J.-P. Bibring, Y. Langevin, F. Altieri, G. Bellucci, B. Gondet, and Mars Express OMEGA Team (2007a), Nature and composition of the icy terrains from Mars Express OMEGA observations, *Planet. Space Sci.*, *55*, 113–133.

Douté, S., E. Deforas, F. Schmidt, R. Oliva, and B. Schmitt (2007b), A comprehensive numerical package for the modeling of Mars hyperspectral images, *Lunar Planet. Sci.*, *XXXVIII*, Abstract 1836.

Durbha, S., R. King, and N. Younan (2007), Support vector machines regression for retrieval of leaf area index from multiangle imaging spectroradiometer, *Remote Sens. Environ.*, *107*, 348–361.

Hapke, B. (1993), Theory of reflectance and emittance spectroscopy, in *Topics in Remote Sensing*, pp. 181–236, Cambridge Univ. Press, Cambridge, U. K.

Hapke, B. (2002), Bidirectional reflectance spectroscopy: 5. The coherent backscatter opposition effect and anisotropic scattering, *Icarus*, *157*, 523–534.

Hastie, T., R. Tibshirani, and J. Friedman (2003), *The Elements of Statistical Learning: Data Mining, Inference, and Prediction*, Springer, New York.

Kimes, D., Y. Knyazikhin, J. Privette, A. Abuegasim, and F. Gao (2000), Inversion methods for physically-based models, *Remote Sens. Rev.*, *18*, 381–439.

Li, K. (1991), Sliced inverse regression for dimension reduction, *J. Am. Stat. Assoc.*, *86*, 316–327.

Murchie, S., et al. (2007), Compact reconnaissance imaging spectrometer for Mars (CRISM) on Mars reconnaissance orbiter (MRO), *J. Geophys. Res.*, *112*, E05S03, doi:10.1029/2006JE002682.

Philpot, W., et al. (2004), Bottom characterization from hyperspectral image data, *Oceanography*, *17*(2), 76–85.

Pragnère, A., F. Baret, M. Weiss, R. Myneni, Y. Knyazikhin, and L. Wang (1999), Comparison of three radiative transfer model inversion techniques to estimate canopy biophysical variables from remote sensing data, *IEEE Trans. Geosci. Remote Sens.*, *2*, 1093–1095.

Schmidt, F., S. Douté, and B. Schmitt (2007), WAVANGLET: An efficient supervised classifier for hyperspectral images, *IEEE Trans. Geosci. Remote Sens.*, *45*, 1374–1385.

Scholkopf, B., and A. J. Smola (2002), *Learning With Kernels: Support Vector Machines, Regularization, Optimization, and Beyond*, MIT Press, Cambridge, Mass.

Shkuratov, Y., L. Starukhina, H. Hoffmann, and G. Arnold (1999), A model of spectral albedo of particulate surfaces: Implications for optical properties of the moon, *Icarus*, *137*, 235–246.

Tarantola, A. (2005), *Inverse Problem Theory and Model Parameter Estimation*, Soc. Ind. Appl. Math., Philadelphia, Pa.

Vincendon, M., Y. Langevin, F. Poulet, J.-P. Bibring, B. Gondet, D. Jouglet, and OMEGA Team (2008), Dust aerosols above the south polar cap of Mars as seen by OMEGA, *Icarus*, *196*, 488–505, doi:10.1016/j.icarus.2007.11.034.

Weiss, M., F. Baret, R. Myneni, A. Pragnère, and Y. Knyazikhin (2000), Investigation of a model inversion technique to estimate canopy biophysical variables from spectral and directional reflectance data, *Agronomie*, *20*, 3–22.

C. Bernard-Michel, M. Fauvel, L. Gardes, and S. Girard, MISTIS, INRIA Rhône-Alpes, Montbonnot, Inovallée, 655 avenue de l'Europe, F-38334 Saint Ismier CEDEX, France.

S. Douté, Laboratoire de Planétologie de Grenoble, Bâtiment D de Physique, B.P. 53, F-38041 Grenoble CEDEX 9, France. (sylvain.doute@obs.ujf-grenoble.fr)